

# CORE-Seg: Reasoning-Driven Segmentation for Complex Lesions via Reinforcement Learning

Yuxin Xie<sup>1</sup>, Yuming Chen<sup>1</sup>, Yishan Yang<sup>1</sup>, Yi Zhou<sup>1</sup> (✉), Tao Zhou<sup>2</sup>, Zhen Zhao<sup>3</sup>, Jiacheng Liu<sup>3</sup>, Huazhu Fu<sup>4</sup>

© The Author(s) 2026.

**Abstract** Medical image segmentation is undergoing a paradigm shift from conventional visual pattern matching to cognitive reasoning analysis. Although Multimodal Large Language Models (MLLMs) have shown promise in integrating linguistic and visual knowledge, significant gaps remain: existing general MLLMs possess broad common sense but lack the specialized visual reasoning required for complex lesions, whereas traditional segmentation models excel at pixel-level segmentation but lack logical interpretability. In this paper, we introduce ComLesion-14K, the first diverse Chain-of-Thought (CoT) benchmark for reasoning-driven complex lesion segmentation. To accomplish this task, we propose CORE-Seg, an end-to-end framework integrating reasoning with segmentation through a Semantic-Guided Prompt Adapter. We design a progressive training strategy from SFT to GRPO, equipped with an adaptive dual-granularity reward mechanism to mitigate reward sparsity. Our Method achieves state-of-the-art results with a mean Dice of 37.06% (14.89% higher than the second-best baseline), while reducing the failure rate to 18.42%. Project Page: [link](#).

**Keywords** Lesion Segmentation, Multimodal Reasoning, Multimodal Foundation Models, Reinforcement Learning

- 1 School of Computer Science and Engineering, Southeast University, Nanjing, 211189, China. E-mail: silver\_iris@163.com; 220252314@seu.edu.cn; ysyang0327@seu.edu.cn; yizhou.szcn@gmail.com (✉).
- 2 School of Computer Science and Engineering, Nanjing University of Science and Technology, Nanjing, 210094, China. E-mail: taozhou.ai@gmail.com.
- 3 Zhongda Hospital, Southeast University, Nanjing, 210009, China. E-mail: zhaozhen8810@126.com; jiachengliu@seu.edu.cn.
- 4 Institute of High-Performance Computing, Agency for Science, Technology and Research, 138632, Singapore. E-mail: hzfu@ieee.org.

Manuscript received: 2026-02-24.

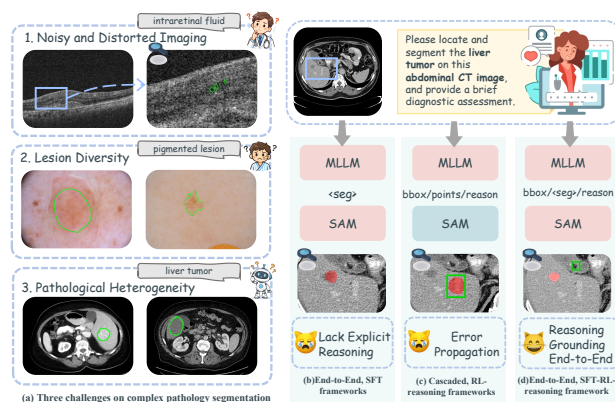


**Fig. 1** (a) Three major challenges in complex medical lesion segmentation, containing noisy and distorted imaging, lesion diversity, and pathological heterogeneity. (b) Supervised finetuned, end-to-end dense prediction architecture. (c) Reinforcement learning-driven, cascaded reasoning framework. (d) Our proposed end-to-end complex-lesion-centric reasoning segmentation framework, CORE-Seg.

## 1 Introduction

Medical image segmentation [1–4] is a core task of clinical diagnosis and treatment planning. However, conventional methods are confined to extracting visual patterns from input images, unable to model the cognitive reasoning process of clinicians. Consequently, these models often perform poorly when segmenting complex or ambiguous lesions that require expert judgment. Recently, Multimodal Large Models (MLLMs) [5–9] have triggered a paradigm shift by combining visual perception with linguistic understanding, enabling more intelligent segmentation systems.

Despite the promising potential of MLLMs, current research [10–14] often prioritizes commonsense reasoning and organ segmentation, while overlooking reasoning-driven segmentation of complex lesions. For instance, tasks like “find the organ damaged by smoking”, rely mostly on commonsense knowledge rather than on reasoning from specific visual cues, which limits their clinical value. Moreover, many studies

focus on anatomical organs segmentation, which typically exhibit fixed locations and clear boundaries, presenting relatively low difficulty. In contrast, complex lesion regions that truly necessitate reasoning and are vital for diagnosis, have received less attention. Consequently, the research focus should shift from *commonsense-based organ segmentation* to *visual-reasoning-based complex lesion segmentation*.

In this paper, we address this gap by targeting **Complex Lesion Segmentation**, a scenario where visual cues are intricate and reasoning is indispensable. As illustrated in Fig. 1(a), unlike the anatomical structures and apparent lesions targeted by current methods, complex lesions present a triad of challenges: (1) *Noisy and Distorted Imaging*: Degraded visual quality caused by acquisition noise and artifacts undermines stable feature extraction. (2) *Lesion Diversity*: Significant variations in lesion shape, location, and boundary limit the generalization of pattern-matching approaches. (3) *Pathological Heterogeneity*: Poor contrast and blurred lesion boundaries obscure the separation between targets and background. These characteristics result in uncertain visual evidence that impedes the stable perception of conventional pattern-matching models. To systematically solve these challenges and facilitate the paradigm shift, we introduce **ComLesion-14K**, the first large-scale, Chain-of-Thought (CoT) driven benchmark explicitly designed for such scenarios. This benchmark comprises 14k cases across 31 diseases, selected from 300k images to focus on scenarios where conventional models often fail.

With this challenging benchmark in place, the limitations of existing solutions become even more apparent. Existing MLLM-based solutions generally follow two technical paths, yet both face significant hurdles in complex lesion segmentation. The first is the supervised finetuned (SFT), end-to-end dense prediction architecture (Fig. 1(b), e.g., LISA[15], MedPLIB[11]). Although achieving a unified pipeline, its reasoning process is often implicit, obscuring crucial decision steps. Consequently, these models lack explainability and struggle with ambiguous lesions that require deep semantic analysis. The second is the reinforcement learning-driven, cascaded reasoning framework (Fig. 1(c), e.g., Seg-Zero[16], MedReasoner[12]). It typically leverages the Group Relative Policy Optimization (GRPO) paradigm[17] to enhance its reasoning capability by optimizing policies based on group-relative rewards. In this pipeline, the MLLM first generates a bounding box, which is then used as a prompt for a downstream segmenter such as SAM[18]. However, this fragmented design suffers from severe error propagation—the final segmentation result is highly dependent on the initial localization accuracy, which is unreliable for complex clinical cases.

To overcome these limitations, we introduce **CORE-Seg, an end-to-end Complex-lesion-centric REasoning Segmentation architecture** (Fig. 1(d)). CORE-Seg integrates the coherence of end-to-end models with the explicit reasoning of reinforcement learning, avoiding the fragmentation and implicit logic of prior methods. Specifically, we introduce a Semantic-Guided Prompt Adapter to project the hidden states of special <seg> tokens from the MLLM’s textual space into SAM’s visual feature space, removing box-based error propagation. Furthermore, we tailor a progressive training pipeline evolving from SFT to GRPO for complex reasoning scenarios. Crucially, we design an adaptive reward mechanism that overcomes reward sparsity to simultaneously enhance multi-lesion reasoning, detection, and segmentation. By combining the interpretability of reasoning-driven learning with the robustness of end-to-end prediction, CORE-Seg achieves superior segmentation accuracy and strong clinical reliability under complex lesion conditions.

The key contributions of this work are fourfold:

- (1) We define a new task paradigm—**Complex Lesion Segmentation**, which necessitates reasoning-driven understanding of lesion regions characterized by high visual ambiguity and heterogeneity.
- (2) A first complex lesion segmentation benchmark, **ComLesion-14K**, is constructed that systematically mines clinical scenarios where existing models usually fail to localize lesions. By simultaneously incorporating the CoT, we bridge the gap for interpretable complex medical image segmentation.
- (3) We propose **CORE-Seg**, an end-to-end reasoning framework anchored by a **Semantic-Guided Prompt Adapter**. This module bridges MLLM reasoning with visual segmentation to eliminate cascading errors. Furthermore, we devise a **progressive SFT-to-GRPO pipeline** and an **adaptive dual-granularity reward mechanism**, effectively resolving reward sparsity while ensuring precise and interpretable predictions.
- (4) CORE-Seg establishes a new state-of-the-art in complex lesion segmentation. Extensive experiments demonstrate that our framework outperforms leading baselines by a significant margin (achieving 37.06% mDice, a +14.89% improvement), while drastically reducing the failure rate to 18.42%.

## 2 Related Work

### 2.1 Multimodal Medical Segmentation Benchmarks

With the rapid advancement of MLLMs, a multitude of reasoning methods and Visual Question Answering (VQA)

datasets have swiftly emerged in both natural[9, 19] and medical domains[11, 20–22]. In the field of medical image segmentation, large-scale datasets such as SA-Med2D-20M[23] and IMed-361M[24] serve as foundational visual corpora for instruction tuning. BiomedParseData[25] features 6.2M image-mask-text triplets for referring segmentation, yet it is limited to explicit naming and lacks reasoning support. U-MRG-14K [12] is the first cross-modal medical dataset to integrate implicit clinical queries, CoT reasoning traces, and pixel-level masks across 14k samples. However, reasoning benchmarks are often confined to single-target organs, while referring datasets lack explanatory capabilities. This creates a gap in reasoning analysis of complex multi-focal lesions. To address this, we propose the ComLesion-14K dataset with CoT annotations for diverse lesion study and multi-target segmentation.

## 2.2 Reasoning-Enhanced Visual Grounding

In recent years, specialist models like nnU-Net[3] and MERIT[4] have achieved remarkable performance but suffer from poor generalization and weak interpretability. The advent of foundation models (e.g., CLIP[26], SAM[18]) facilitated referring segmentation approaches such as BiomedParse[25] and CLIP-Driven Universal Model[27]. While these methods utilize text for guidance, they function primarily as recognition modules, failing to provide rational explanations for their decisions.

The rise of Large Language Models has broken this bottleneck. Inspired by LISA[15], which endowed segmentation with reasoning capabilities, medical reasoning models have rapidly evolved. For instance, MedPLIB[11] pioneered pixel-level reasoning via a multi-expert strategy, while MediSee[10] incorporated logic-driven constraints for superior performance. However, these methods often rely heavily on instruction tuning, making them prone to overfitting. Crucially, they lack the capability to generate explicit reasoning processes for complex scenarios—a limitation our work aims to address.

## 2.3 Reinforcement Learning for Image Segmentation

Reinforcement Learning (RL) has emerged as a pivotal technique for aligning models with human intent. The methodology has evolved from Proximal Policy Optimization(PPO)[28] to Direct Preference Optimization(DPO)[29], with Group Relative Policy Optimization (GRPO)[17] further enhancing computational efficiency. However, in the segmentation domain, existing approaches such as Seg-Zero[16], SAM-R1[30], MedReasoner[12] adopt a serial architecture. This disjointed paradigm decouples the reasoning module from the

segmentation head, leading to error propagation and inconsistent optimization. To address these limitations, inspired by LENS[31], we propose a unified end-to-end framework that integrates Supervised Fine-Tuning (SFT) with GRPO. This approach enables the joint optimization of explicit medical reasoning and pixel-level segmentation.

## 3 ComLesion-14K Dataset

Most existing datasets for medical image segmentation typically focus on specific modalities with fixed labels. While recent studies have introduced visual prompts (e.g., points, boxes) or text guidance (e.g., U-MRG[12], MLMR-SD[10]), they mainly target organ-level structures, overlooking the pathological details required for lesion identification. Complex lesion segmentation is clinically critical yet more challenging due to subtle boundaries and intricate anatomical contexts.

To bridge this gap, we introduce **ComLesion-14K**, a multimodal dataset specifically designed for complex lesion segmentation. Unlike existing works, it incorporates explicit reasoning chains that mimic the clinician’s diagnosis process—identifying global context, localizing lesions, and delineating boundaries. The construction pipeline comprises three stages, as illustrated in Fig. 2(a).

### 3.1 Data Selection and Difficulty-Aware Filtering

To curate a subset of complex samples that challenge current segmentation models, we aggregated raw data from 26 public datasets authorized for redistribution. Instead of applying a static filtering threshold, we configured a **difficulty-aware filtering mechanism**.

We first trained multiple U-Net[1] models on each dataset to vote for selection. We hypothesize that the distribution of segmentation errors (measured by  $1 - \text{Dice}$ ) follows a heavy-tailed distribution, where the tail represents the complex cases of interest. We modeled this error distribution using a power-law function as:

$$p(x) \propto x^{-\alpha}, \quad x \geq x_{\min}, \quad (1)$$

where  $x$  represents the segmentation error and  $\alpha$  is the scaling parameter estimated using the Clauset method[32]. To determine the optimal threshold  $x_{\min}$  that separates trivial noise from hard cases, we utilized the Kneedle algorithm[33] to detect the knee point of the fitted curve. This statistical approach allows for an adaptive and interpretable selection process across datasets with varying difficulty levels, filtering out simple cases and retaining those with high morphological variability or low contrast (see Fig. 1(a)). Finally, manual spot-checks were conducted to verify that the selected samples

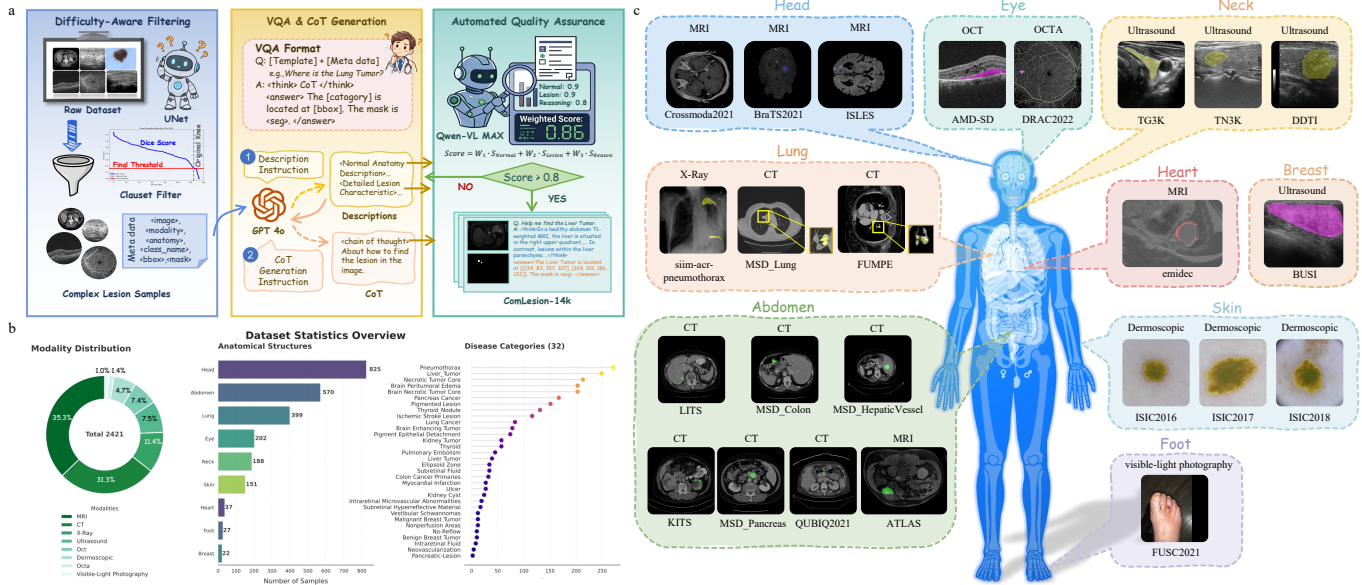


**Fig. 2 Overview of the ComLesion-14K dataset construction and composition.** (a) The dataset construction pipeline, including difficulty-aware filtering to select complex lesion samples, VQA and CoT generation for structured descriptions and reasoning, and automated quality assurance to ensure annotation consistency and reliability. (b) Dataset statistics summarizing the distribution of imaging modalities, anatomical structures, and disease categories. (c) Representative samples illustrating broad organ coverage across diverse imaging modalities.

are primarily characterized by pathological complexity, effectively ruling out instances of annotation errors or omissions.

### 3.2 CoT and VQA Generation

For each sample, we construct a structured tuple  $\mathcal{D} = \{I, M, Q, R, A\}$ . Here,  $I$  and  $M$  denote the raw image and segmentation mask. The textual components  $Q, R, A$  are derived from metadata (modality, anatomy, disease category) and bounding boxes extracted from  $M$ .

The clinical queries  $Q$  are synthesized using **dynamic templates** to ensure linguistic diversity. The answers  $A$  strictly follow the format: “The {lesion} is located at {bbboxes}.”, serving as direct supervision for localization.

To generate high-quality reasoning text  $R$ , we leveraged GPT-4o [9] with a two-step prompting strategy:

- **Step 1: Visual Perception Simulation.** Conditioned on the metadata, the model generates a **concise description** of the normal anatomical context and a **detailed characterization** of the lesion (e.g., specific location, irregular shape, heterogeneous texture). This simulates the initial observation of a clinician.
- **Step 2: Visual Reasoning for Localization.** Given the target disease, this step focuses on the reasoning process of identification. The model leverages evidence from Step 1 to deduce the precise spatial location, explicitly explaining how to distinguish the target area from the surrounding background and confounders.

Crucially, explicit coordinate values are stripped from the final  $R$ . This constraint prevents the model from shortcut learning via numerical regression, forcing it to rely on semantic-level anatomical understanding.

### 3.3 Automated Quality Assurance

To guarantee the logical consistency of the generated text, we established an automated review pipeline using Qwen2.5-VL-Max[8]. By decoupling the evaluator from the generator, this design mitigates potential intrinsic biases and stylistic preferences, ensuring that the evaluation results are more objective and reliable. The model scores each sample based on three criteria: normal anatomy description ( $S_{normal}$ ), lesion characterization ( $S_{lesion}$ ), and reasoning logic ( $S_{reason}$ ). The final quality score  $S_{final}$  is calculated as:

$$S_{final} = w_1 \cdot S_{normal} + w_2 \cdot S_{lesion} + w_3 \cdot S_{reason}, \quad (2)$$

where we empirically set weights to  $w_1 = 0.3, w_2 = 0.3, w_3 = 0.4$  to emphasize the importance of logic reasoning. Samples with  $S_{final} < 0.8$  were regenerated.

### 3.4 Dataset Statistics and Distribution

The ComLesion-14K dataset comprises 13678 samples that span 8 imaging modalities, 9 anatomical regions, and 31 disease categories. As shown in Fig. 2 (b)(c), the distribution reflects the availability of clinical data in real-world, with MRI and CT being the dominant modalities (accounting for  $\sim 66\%$

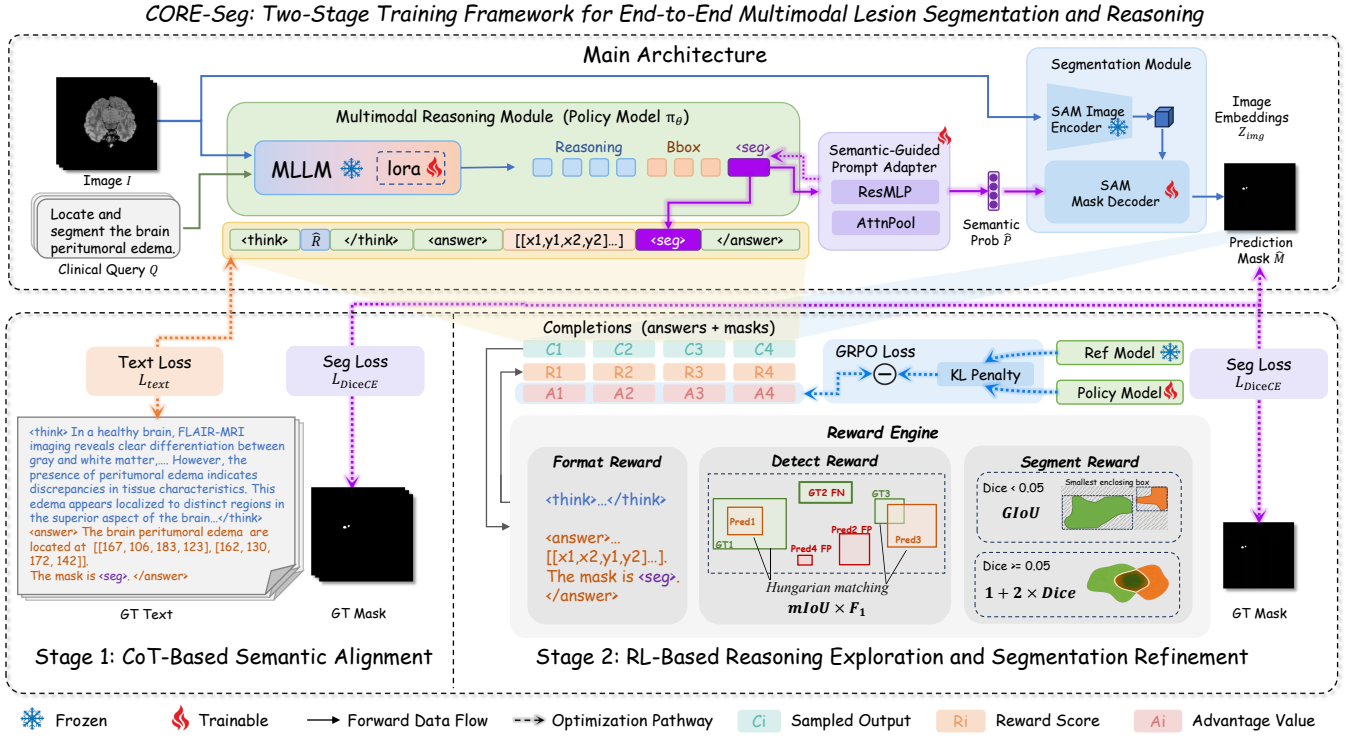


**Fig. 3 Overview of the CORE-Seg framework.** The architecture integrates an MLLM with a SAM via a Semantic-Guided Prompt Adapter. The training consists of two stages: (1) CoT-Based Semantic Alignment Stage: Supervised fine-tuning establishes the mapping between clinical reasoning and lesion localization using the  $\langle \text{seg} \rangle$  token. (2) RL-Based Reasoning Exploration and Segmentation Refinement Stage: The model is further optimized using GRPO. A multi-dimensional Reward Engine (evaluating format, detection, and segmentation) serves as the critic, where a Dual-Granularity Mask Reward penalizes disconnected regions and encourages precise boundary delineation.

of data), and head and abdomen being the primary anatomical regions. Despite this imbalance, the dataset covers a wide spectrum of lesion types, ranging from large organ tumors to subtle retinal lesions, ensuring the model’s robustness across varied scales and contrasts.

## 4 CORE-Seg

Building upon the ComLesion-14K dataset, we propose CORE-Seg, an end-to-end multimodal framework designed for simultaneous complex lesion segmentation and interpretable reasoning. Unlike conventional disjointed pipelines, we introduce a **Semantic-Guided Prompt Adapter** to unify semantic understanding and visual localization into a cohesive system, effectively preventing error propagation. Our training paradigm consists of two distinct stages: a CoT cold-start stage that aligns cross-modal semantics, followed by a reinforcement learning stage driven by an **adaptive dual-granularity reward mechanism** to unlock the model’s reasoning potential and refine segmentation precision.

### 4.1 Unified End-to-End Architecture

As illustrated in Fig. 3, CORE-Seg deviates from multi-stage approaches by establishing a fully differentiable, end-to-end pathway from raw input to final segmentation. The architecture operates through a unified pipeline comprising three components: the Multimodal Reasoning Module, the Semantic-Guided Prompt Adapter, and the Segmentation Module. The reasoning module first interprets the medical context and identifies potential lesions; the adapter then functions as a bridge to translate these semantic insights into visual cues; and finally, the segmentation module executes precise pixel-level delineation based on these cues.

#### 4.1.1 Multimodal Reasoning Module

We employ a MLLM, specifically Qwen-VL-2.5-3B, as the reasoning backbone. Given an input image  $I$  and a clinical query  $Q$ , the model generates a structured output sequence  $\hat{O}$  formatted as:

$$\hat{O} = \langle \text{think} \rangle \hat{R} \langle \text{/think} \rangle \langle \text{answer} \rangle \hat{A} \langle \text{/answer} \rangle \quad (3)$$

Here,  $\hat{R}$  and  $\hat{A}$  are reasoning and answer correspond strictly to the ground-truth  $R$  and  $A$  defined in Sec. 3. Note that, as

defined,  $\hat{A}$  contains the special learnable token  $\langle \text{seg} \rangle$  at its end to trigger the subsequent mask decoder.

The hidden state of this  $\langle \text{seg} \rangle$  token serves as a condensed semantic anchor. Through the attention mechanism of the Transformer, it aggregates information from both the preceding reasoning rationale and the localization cues. Consequently, this token encapsulates a high-level representation of what needs to be segmented and where it roughly is, effectively preparing a semantic-rich query for the subsequent Semantic-Guided Prompt Adapter to retrieve pixel-level visual features.

#### 4.1.2 Semantic-Guided Prompt Adapter

The Semantic-Guided Prompt Adapter bridges the high-level reasoning of the MLLM with pixel-level segmentation. Specifically, we extract the final-layer hidden state of the special  $\langle \text{seg} \rangle$  token as a condensed semantic anchor  $P \in \mathbb{R}^{B \times 1 \times D}$ , where  $B$  denotes the batch size and  $D$  is the hidden dimension of the MLLM. This embedding summarizes the multimodal reasoning outcome and encodes implicit spatial priors. Unlike explicit coordinate prompts (e.g., points or boxes),  $P$  acts as a global semantic descriptor that conditions the segmentation decoder to attend to all regions consistent with the pathological semantics, including multiple spatially separated lesions.

To mitigate the inherent feature distribution discrepancy between the linguistic and visual modalities,  $P$  is first projected into a visually-aligned manifold via stacked Residual MLP (ResMLP) blocks, formulated as:

$$h_{l+1} = h_l + \text{ResMLP}(\text{LayerNorm}(h_l)), \quad (4)$$

where  $h_0 = P$ , and the final output denotes the refined feature  $\tilde{P}$ . Subsequently, to adapt this linguistic feature into a format compatible with the segmentation decoder, we employ an attention-based module introduced with a **learnable query**  $q_{\text{learn}}$ . The query interacts with  $\tilde{P}$  via cross-attention mechanisms to extract and reconstruct the segmentation prompt:

$$\hat{P} = \text{Proj} \left( \text{LayerNorm} \left( \text{Attn}(q_{\text{learn}}, \tilde{P}, \tilde{P}) \right) \right), \quad (5)$$

where  $q_{\text{learn}}$  serves as the query while  $\tilde{P}$  acts as both key and value. The resulting semantic probe  $\hat{P} \in \mathbb{R}^{B \times 1 \times 256}$  is then injected into the segmentation decoder, effectively modulating the mask generation process with precise linguistic guidance.

#### 4.1.3 Segmentation Model

We use the pre-trained Segment Anything Model (SAM)[30] as the segmentation backbone. For an input medical image, the SAM image encoder (e.g., ViT-H) produces image embeddings  $Z_{\text{img}}$ . We then inject the semantic probe  $\hat{P}$  into SAM's prompt pathway. The mask decoder takes  $(Z_{\text{img}}, \hat{P})$  as inputs

and leverages SAM's native two-way attention to fuse prompt and image features, yielding the binary segmentation mask  $\hat{M} \in \mathbb{R}^{H \times W}$ :

$$\hat{M} = \text{SAM}_{\text{Decoder}}(Z_{\text{img}}, \hat{P}). \quad (6)$$

Although SAM can be conditioned by the semantic probe, reliable semantic prompting requires both medical reasoning and robustness. To this end, we propose a two-stage training strategy that first establishes stable semantic-visual alignment and then further enhances generalization and segmentation performance, which we elaborate on in the following sections.

## 4.2 Stage 1: CoT-Based Semantic Alignment

In this cold-start stage, we aim to inject domain-specific medical knowledge and establish a preliminary alignment between linguistic reasoning and visual localization. To achieve this efficiently, we apply Low-Rank Adaptation (LoRA) to the MLLM, enabling it to learn specialized CoT patterns while keeping most parameters frozen. Concurrently, we fine-tune the Semantic-Guided Prompt Adapter and the SAM mask decoder to ensure the semantic  $\langle \text{seg} \rangle$  token is accurately translated into spatial queries for segmentation.

The training is supervised end-to-end using a composite loss function:

$$\mathcal{L}_{S1} = \lambda_1 \mathcal{L}_{\text{txt}}(\hat{O}, R, A) + \lambda_2 \mathcal{L}_{\text{DiceCE}}(\hat{M}, M). \quad (7)$$

Here,  $\mathcal{L}_{\text{txt}}$  is the auto-regressive cross-entropy loss that guides the generation of reasoning, while the combination of Dice and Cross-Entropy loss optimizes pixel-level segmentation precision,  $\{\lambda_i\}_{i=1}^2$  are balancing hyperparameters. This joint optimization empowers the model to simultaneously understand medical semantics and locate lesion boundaries.

## 4.3 Stage 2: RL-Based Reasoning Exploration and Segmentation Refinement

Following the supervised alignment, we introduce reinforcement learning (RL) to enable reasoning exploration and error correction on complex medical cases, while simultaneously refining segmentation boundaries. We employ group relative policy optimization (GRPO)[17] as our core algorithm. Compared to the previous proximal policy optimization (PPO)[28], GRPO is more memory-efficient as it eliminates the need for a critic model, instead estimating the baseline from the group average of sampled outputs. This stability is crucial for fine-tuning large multi-modal models.

### 4.3.1 Reward Function

To guide the optimization effectively, we design a composite reward function  $\mathcal{R}$  tailored for complex medical scenarios.

- **Format Reward** ( $r_{fmt}$ ): This strictly enforces the structural integrity of the reasoning process. To receive a positive reward, the output must follow a specific sequence: a rationale chain enclosed within <think> tags, followed by the final conclusion in <answer> tags. Crucially, the generated text must explicitly contain the special <seg> token to activate the segmentation head; otherwise, the reward is set to zero.
- **Bipartite Matching Reward** ( $r_{bbox}$ ): To ensure robust multi-lesion grounding, we formulate the evaluation as a set prediction problem, aiming to balance localization precision with detection completeness. Given the set of predicted boxes  $\hat{B}$  and ground-truth boxes  $B$ , we first employ the **Hungarian algorithm** to perform optimal bipartite matching, minimizing the global IoU cost. Based on this alignment, we compute the Mean Intersection-over-Union ( $mIoU_{matched}$ ) to quantify spatial accuracy. Furthermore, to rigorously penalize both hallucinations (false positives) and missed diagnoses (false negatives), we modulate the reward using the  $F_1$  score derived from Precision ( $P$ ) and Recall ( $R$ ). The final holistic spatial reward is defined as:

$$r_{bbox} = mIoU_{matched} \times F_1, \text{ where } F_1 = 2 \cdot \frac{P \cdot R}{P + R}. \quad (8)$$

- **Dual-Granularity Mask Reward** ( $r_{mask}$ ): Despite Supervised Fine-Tuning (SFT), the model may struggle with complex lesions, occasionally yielding non-overlapping predictions (i.e., Dice  $\approx 0$ ). This leads to reward sparsity, preventing effective policy updates. To mitigate this, we propose a density-aware adaptive strategy that transitions from coarse-grained box guidance to fine-grained pixel supervision.

We first evaluate the standard Dice coefficient between the predicted mask  $\hat{M}$  and the ground truth  $M$ . To provide directional gradients even when pixel-level overlap is absent, we concurrently compute the Generalized IoU (GIoU) on their derived bounding boxes ( $B_{\hat{M}}, B_M$ ). The metrics are defined as:

$$Dice = \frac{2|\hat{M} \cap M|}{|\hat{M}| + |M|}, \quad (9)$$

$$GIoU = IoU_{bbox} - \frac{|C \setminus (B_{\hat{M}} \cup B_M)|}{|C|}, \quad (10)$$

where  $C$  is the smallest enclosing convex hull covering both boxes. The final adaptive reward is formulated as:

$$r_{mask} = \begin{cases} GIoU(B_{\hat{M}}, B_M), & \text{if } Dice < 0.05 \\ 1 + \lambda \cdot Dice, & \text{otherwise} \end{cases} \quad (11)$$

Here, we set  $\lambda = 2$  to amplify the reward for high-quality segmentations. We empirically selected 0.05 as the threshold to guarantee informative gradients for non-overlapping predictions where Dice loss becomes ineffective. This mechanism ensures valid reward signal via GIoU during early training stages or difficult samples, while prioritizing pixel-perfect precision once approximate localization is achieved.

#### 4.3.2 Training Objective

The final objective combines the RL policy gradient with the supervised segmentation loss. For each  $(I, Q)$ , the policy model  $\pi_\theta$  rolls out a group of responses  $\{C_i\}_{i=1}^G$  (containing MLLM outputs  $\hat{O}$  and mask prediction  $\hat{M}$ ) with the group size  $G$ , and we compute a GRPO loss  $L_{GRPO}$  using our composite reward function  $\mathcal{R}$  and KL divergence regularization  $\mathbb{D}_{KL}$ . In parallel, the predicted masks are supervised against the ground truth to ensure precise segmentation.

$$\mathcal{L}_{S2} = \lambda_3 \mathcal{L}_{GRPO}(\pi_\theta; \mathcal{R}, \mathbb{D}_{KL}) + \lambda_4 \mathcal{L}_{DiceCE}(\hat{M}, M). \quad (12)$$

$\{\lambda_i\}_{i=3}^4$  are balancing hyperparameters. By jointly optimizing these objectives, the model iteratively self-refines its reasoning chains and boundary predictions in a stable and robust manner.

## 5 Experiments

### 5.1 Data and Experimental Setup

#### 5.1.1 Datasets

We evaluate our method on the ComLesion-14K dataset, which is described in detail in Sec. 3. For the MLLM input, all images are resized so that the longer edge is at most 512 pixels while preserving the aspect ratio. For the SAM input, images are resized to  $512 \times 512$ . We randomly sample 2,421 image-text-mask triplets for the test set, and use the remaining data for training.

To further assess the generalization of our two-stage training strategy, we categorize Out-of-Domain (OOD) benchmarks into three levels by the severity of distribution shift: (1) TNSCUI2020[34] (Ultrasound thyroid nodule): For evaluating basic distribution shifts. (2) ISPY[35] (MRI breast tumor): With an unseen novel lesion class. (3) CVC-ClinicDB[36] (Endoscopic polyp): The most challenging, with domain gaps in both imaging modality and semantic class.

#### 5.1.2 Implementation Details

Our framework utilizes Qwen2.5-VL-3B[8] as the reasoning backbone and MedSAM 2[42] for segmentation, implemented on 2 NVIDIA A6000 GPUs using AdamW optimizer with DeepSpeed acceleration. We employ LoRA ( $r = 64, \alpha = 128, \text{dropout} = 0.05$ ) for the MLLM, while fully fine-tuning

**Table 1 Quantitative comparison on complex lesion segmentation.** We report mDice, mIoU, and Failure Rate (Fail). Detailed Dice scores for 9 anatomical regions are provided to analyze local grounding capabilities. All values are in percentage (%). Best results are **bolded**, second best are underlined.

| Method                          | Overall Performance (%) |                 |                   | Anatomy-specific Dice (%) |              |              |             |              |              |              |              |              |
|---------------------------------|-------------------------|-----------------|-------------------|---------------------------|--------------|--------------|-------------|--------------|--------------|--------------|--------------|--------------|
|                                 | mDice $\uparrow$        | mIoU $\uparrow$ | Fail $\downarrow$ | Head                      | Abd.         | Lung         | Eye         | Neck         | Skin         | Foot         | Breast       | Heart        |
| <b>General MLLMs</b>            |                         |                 |                   |                           |              |              |             |              |              |              |              |              |
| Qwen2.5-VL-72B [8]              | 11.04                   | 7.78            | 37.61             | 6.68                      | 5.11         | 3.30         | 5.23        | 31.36        | 54.09        | 22.89        | <u>52.86</u> | 1.21         |
| InternVL3-8B [37]               | 4.18                    | 2.72            | 73.90             | 2.36                      | 0.50         | 0.79         | 0.96        | 11.34        | 31.44        | 5.55         | 14.07        | 0.86         |
| Qwen2.5-VL-7B [8]               | 8.30                    | 5.56            | 42.76             | 3.62                      | 4.47         | 2.62         | 2.89        | 23.79        | 48.12        | 5.18         | 41.43        | 3.06         |
| <b>Medical-Specific MLLMs</b>   |                         |                 |                   |                           |              |              |             |              |              |              |              |              |
| HuatuoGPT-7B [6]                | 4.73                    | 3.04            | 43.72             | 3.58                      | 1.88         | 2.02         | 3.20        | 13.49        | 20.13        | 0.10         | 16.11        | 0.62         |
| Chiron-o1-8B [38]               | 3.35                    | 2.19            | 66.61             | 2.35                      | 0.81         | 1.50         | 1.86        | 9.60         | 14.74        | 1.80         | 28.01        | 0.84         |
| Lingshu-7B [39]                 | 7.37                    | 4.73            | 58.41             | 3.34                      | 4.62         | 2.60         | 3.27        | 22.56        | 37.76        | 6.01         | 26.61        | 0.88         |
| MedGemma-4B [40]                | 6.03                    | 3.85            | 49.11             | 3.10                      | 1.95         | 2.39         | 2.30        | 19.09        | 34.15        | 4.08         | 25.99        | 1.98         |
| <b>Grounding-Specific MLLMs</b> |                         |                 |                   |                           |              |              |             |              |              |              |              |              |
| SegZero-7B [16]                 | 9.08                    | 6.23            | <u>19.84</u>      | 4.72                      | 2.49         | 3.72         | 3.15        | 25.87        | 54.57        | 7.53         | 50.33        | 2.92         |
| VLMR1-REC-3B [41]               | 4.76                    | 2.99            | 24.98             | 4.45                      | 1.14         | 2.76         | 3.50        | 11.74        | 15.65        | 1.69         | 32.77        | 1.27         |
| MedPLIB-7B [11]                 | 12.90                   | 8.77            | 42.40             | 12.51                     | 6.00         | 4.12         | 4.82        | 22.11        | 44.45        | <b>48.34</b> | 44.85        | 3.20         |
| MediSee-7B [10]                 | 11.07                   | 7.49            | 55.97             | <u>21.18</u>              | 4.01         | 4.00         | 1.20        | 5.16         | 22.98        | 9.90         | 5.58         | <u>9.84</u>  |
| LISA-3B (Trained) [15]          | <u>22.17</u>            | <u>16.49</u>    | 44.28             | 16.39                     | <u>22.71</u> | <u>19.40</u> | 5.64        | 35.51        | <u>66.20</u> | 17.89        | 48.21        | 2.39         |
| SegZero-3B (Trained) [16]       | 17.47                   | 12.28           | 52.57             | 13.41                     | 13.94        | 14.37        | <b>8.72</b> | <u>40.64</u> | 53.54        | <u>39.51</u> | 21.78        | <b>12.21</b> |
| <b>CORE-Seg (Ours)</b>          | <b>37.06</b>            | <b>27.79</b>    | <b>18.42</b>      | <b>31.40</b>              | <b>39.56</b> | <b>41.40</b> | <u>8.28</u> | <b>47.25</b> | <b>74.85</b> | 37.53        | <b>70.99</b> | 8.14         |

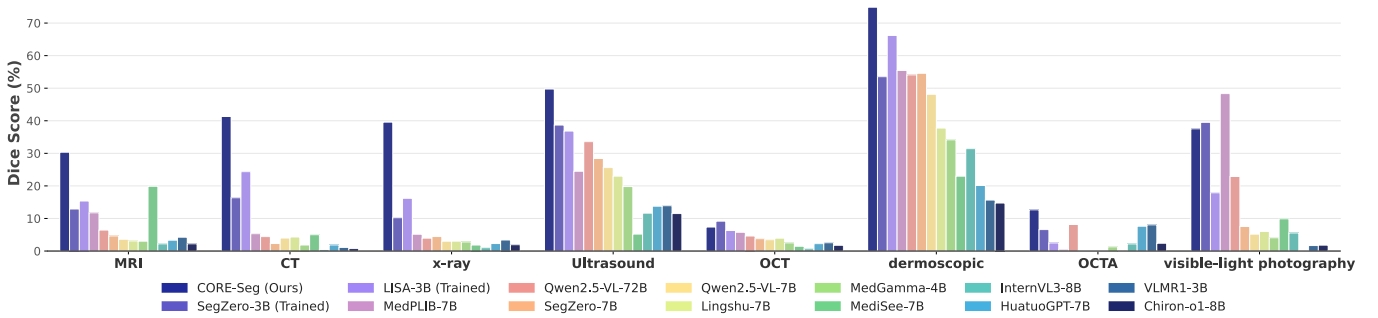


**Fig. 4 Comparison of mDice scores across 8 medical modalities.** CORE-Seg demonstrates superior generalization capabilities, achieving state-of-the-art performance particularly in MRI, CT, X-Ray and Ultrasound.

the Semantic-Guided Prompt Adapter and Mask Decoder. The training proceeds in two stages. In the first stage, we train for 1 epoch with a batch size of 32 and a learning rate of  $1e-4$ . In the second stage, we fine-tune for 2 epochs with a reduced learning rate of  $5e-6$  and a batch size of 16. The sampling number is set to 4. The loss weights  $\{\lambda_i\}_{i=1}^4$  are empirically set to 1.0.

### 5.1.3 Evaluation Metrics

To comprehensively assess segmentation quality and system robustness, we employ the **Dice Similarity Coefficient (Dice)** and **Intersection over Union (IoU)** to measure the spatial overlap between predicted masks and ground truth. However, given the high complexity of lesion segmentation tasks, standard MLLMs are prone to severe hallucinations or instruction-following failures. To explicitly quantify such instability, we introduce the **Failure Rate** as a critical reliability

metric. A prediction is classified as a failure if: (1) the resulting Dice score is 0 (indicating a complete loss of visual grounding), or (2) the MLLM generates an output with an invalid format.

## 5.2 Complex Lesion Reasoning Segmentation Results

To comprehensively validate CORE-Seg, we conduct extensive comparisons with a wide array of state-of-the-art models across three categories: (1) **General MLLMs**: Qwen2.5-VL-72B[8], Qwen2.5-VL-7B, and InternVL3-8B[37]; (2) **Medical-Specific MLLMs**: HuatuoGPT-7B[6], Chiron-o1-8B[38], Lingshu-7B[39], and MedGemma-4B[40]; and (3) **Grounding-Specific MLLMs**: SegZero-7B[16], VLMR1-REC-3B[41], MedPLIB-7B[11], and MediSee-7B[10]. Specifically, the models above are evaluated in a zero-shot manner to assess their intrinsic medical adaptability using

their official pre-trained weights. Furthermore, for a strictly fair comparison, we fine-tuned LISA-3B[15] and SegZero-3B[16] aligning them with the same Qwen2.5-VL-3B backbone and MedSAM2 to validate our framework advantages.

### 5.2.1 Overall Performance

In Table 1, CORE-Seg establishes a new state-of-the-art(SOTA) for complex lesion segmentation with **37.06% mDice** and **27.79% mIoU**, outperforming the second-best LISA-3B by +14.89%. While General and Medical MLLMs suffer high failure rates due to weak grounding alignment, CORE-Seg maintains the lowest rate at **18.42%**.

Notably, existing grounding models (MedPLIB, MediSee) show limited performance ( $\sim 12\%$  mDice) due to scarce lesion samples in their organ-centric training data, verifying the necessity of our lesion-targeted model. Moreover, comparisons highlight our architectural advantages: SFT-based LISA has a high failure rate (44.28%) and is prone to overfitting; cascaded SegZero matches our low failure rate but suffers low accuracy from multi-stage error accumulation. Ultimately, CORE-Seg proves an end-to-end RL-driven paradigm effectively balances precise localization and generalization.

### 5.2.2 Anatomical and Modal Analysis

As shown in Table 1 and Fig. 4, CORE-Seg exhibits strong cross-distribution robustness in complex lesion segmentation: it outperforms baselines in 6 of 9 anatomical categories, adapts well to grayscale radiology modalities (MRI/CT) where general MLLMs fail, and maintains robust segmentation in high-noise modalities (Ultrasound/OCT), validating the universal feature enhancement of its reasoning mechanism.

### 5.2.3 Parameter Efficiency Analysis

Crucially, CORE-Seg achieves SOTA performance with exceptional efficiency. Built upon a compact 3B backbone optimized via PEFT (LoRA), our model operates with minimal trainable parameters and computational overhead. Despite being  $24\times$  smaller than the massive Qwen2.5-VL-72B, CORE-Seg surpasses it by 26.02% in mDice. This economical training strategy proves that explicit reasoning alignment outweighs sheer parameter scaling, enabling rapid deployment for complex medical segmentation even in resource-constrained clinical environments.

## 5.3 Ablation Study

### 5.3.1 Ablation Study on Progressive Framework

Table 2 quantifies the efficacy of our progressive design by dissecting module and training stage contributions from two perspectives.

**Table 2 Ablation study on progressive framework.** We report mDice, mIoU, and Failure Rate (Fail) on In-Distribution (ID) data. For Out-Of-Distribution (OOD) robustness, we report mDice and Fail across three challenging datasets: CVC-ClinicDB, TN-SCUI, and ISPY.

| Components   |              |              | ID Performance   |                 |                   | OOD Robustness (mDice $\uparrow$ /Fail $\downarrow$ ) |                   |                    |
|--------------|--------------|--------------|------------------|-----------------|-------------------|---|-------------------|--------------------|
| SG-A         | S1           | S2           | mDice $\uparrow$ | mIoU $\uparrow$ | Fail $\downarrow$ | CVC-ClinicDB  | TN-SCUI           | ISPY               |
| -            | -            | -            | 4.86             | 3.00            | 58.5              | 30.35/27.6  | 15.01/37.8        | 0.98/65.2          |
| -            | $\checkmark$ | -            | 23.60            | 16.57           | 45.2              | 37.67/26.2  | 50.26/14.4        | 32.26/21.6         |
| $\checkmark$ | $\checkmark$ | -            | 30.37            | 22.20           | 26.02             | 34.16/17.20   | 64.16/1.60        | 29.31/15.40        |
| $\checkmark$ | $\checkmark$ | $\checkmark$ | <b>37.06</b>     | <b>27.79</b>    | <b>18.42</b>      | <b>48.20/15.00</b>                                    | <b>74.82/2.20</b> | <b>38.71/13.00</b> |

**Table 3 Ablation study of adaptive reward mechanism in CORE-Seg.** We analyze the impact of training-time reasoning guidance, including CoT, thinking format reward, reward types (bbox/mask), and Dice loss.

| CoT          | $r_{fmt}$    | $r_{bbox}$   | $r_{mask}$   | $L_{DiceCE}$ | mDice $\uparrow$ | mIoU $\uparrow$ | Fail $\downarrow$ |
|--------------|--------------|--------------|--------------|--------------|------------------|-----------------|-------------------|
| -            | -            | -            | -            | -            | 31.24            | 23.15           | 20.08             |
| $\checkmark$ | -            | -            | -            | -            | 30.37            | 22.20           | 26.02             |
| $\checkmark$ | $\checkmark$ | $\checkmark$ | -            | -            | 26.87            | 18.91           | 30.08             |
| $\checkmark$ | $\checkmark$ | -            | $\checkmark$ | -            | 31.83            | 23.45           | 24.63             |
| $\checkmark$ | $\checkmark$ | $\checkmark$ | $\checkmark$ | -            | 32.41            | 24.06           | 24.32             |
| $\checkmark$ | $\checkmark$ | $\checkmark$ | $\checkmark$ | $\checkmark$ | <b>37.06</b>     | <b>27.79</b>    | <b>18.42</b>      |

First, We evaluate the Semantic-Guided Prompt Adapter (SG-A) on the in domain dataset. In SFT-Stage(S1), replacing SG-A with a simple *Linear layer* drops mDice from 30.37% to 23.60%, demonstrating that SG-A is essential for aligning semantic priors whereas naive projections are insufficient. However, relying solely on SFT tends to overfit the training distribution, limiting performance on complex cases. Subsequently, incorporating RL-Stage(S2) boosts mDice to 37.06% and minimizes the failure rate to 18.42%, confirming that S2 significantly enhances generalization, effectively refining details.

Second, we test OOD robustness on TN-SCUI, ISPY and CVC-ClinicDB(as Sec. 5.1.1 describes). S1 has basic capabilities but overfits the source domain, restricting generalization. As shown in Table 2, despite the increasing severity of domain shifts across these datasets, S2 consistently outperforms the SFT baseline by approximately 10% mDice (e.g., +10.66% on TN-SCUI, +9.4% on ISPY, and +14.04% on CVC-ClinicDB). This improvement confirms that the exploration mechanism in RL is critical for overcoming SFT-induced overfitting, enabling the model to learn robust, transferable policies.

### 5.3.2 Ablation Study on Adaptive Reward Mechanism

This ablation study verifies the adaptive reward mechanism of CORE-Seg from two perspectives: reasoning validity and optimization strategy design.

We first examine whether explicitly introducing reasoning benefits segmentation. Under the SFT-only setting (Line 1–2), adding CoT slightly decreases mDice by 0.87%, indicating that static training lacks sufficient optimization signals to exploit reasoning. In contrast, when applying GRPO (Line

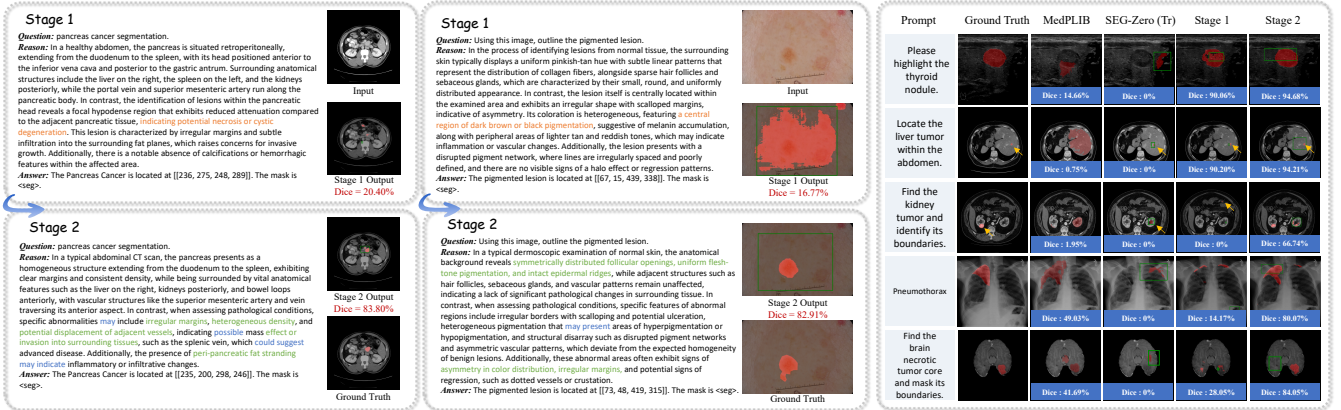


**Fig. 5** Qualitative results of our two-stage method and baselines. Stage 2 refines Stage 1 with more image-grounded reasoning, improving mask quality and robustness, especially for small lesions and imperfect box localization.

**Table 4** Ablation study on the semantic probe selection. We compare using the specific `<seg>` token (Ours) versus the hidden states of the whole answer across training stages.

| Semantic Probe                 | Training Stage | mDice $\uparrow$ | mIoU $\uparrow$ | Fail $\downarrow$ |
|--------------------------------|----------------|------------------|-----------------|-------------------|
| Whole Answer                   | S1             | 32.25            | 23.90           | 24.82             |
|                                | S1+S2          | 33.01            | 24.54           | 24.32             |
| <code>&lt;seg&gt;</code> Token | S1             | 30.37            | 22.20           | 26.02             |
|                                | S1+S2          | <b>37.06</b>     | <b>27.79</b>    | <b>18.42</b>      |

**Table 5** Comparison of different SAM backbones. We evaluate the impact of the SAM version in Stage 1.

| Segmentation Model         | mDice $\uparrow$ | mIoU $\uparrow$ | Fail $\downarrow$ |
|----------------------------|------------------|-----------------|-------------------|
| SAMed2D[23]                | 19.58            | 13.44           | 45.28             |
| SAM 2[43]                  | 23.60            | 16.57           | 39.87             |
| <b>MedSAM 2[42] (Ours)</b> | <b>30.37</b>     | <b>22.20</b>    | <b>26.02</b>      |

3–6), reasoning is effectively activated, and the full model achieves 37.06% mDice (+5.82% over the non-reasoning SFT baseline). These results show that reasoning becomes beneficial only when coupled with reward-based policy optimization, validating our reason-to-segment paradigm under reinforcement learning.

We further analyze the impact of different reward configurations during GRPO training. Optimizing with Bipartite Matching Reward  $r_{bbox}$  only, the mDice drops sharply to 26.87%. This suggests that the optimization objective degenerates from segmentation to coarse localization. In contrast, using Dual-Granularity Mask Reward  $r_{mask}$  alone improves mDice to 31.83%, confirming that dense mask-level rewards are essential for accurate segmentation. Incorporating  $r_{bbox}$  on top of  $r_{mask}$  further boosts mDice to 32.41% (+0.58%), indicating that  $r_{bbox}$  complementary spatial guidance and synergistically enhance the prediction of the `<seg>` token. Finally, supplementing both rewards with DiceCE Loss  $L_{dice}$  drives a significant performance gain, with mDice increasing from 32.41% to 37.06% (+4.61%). This is because RL optimization is unstable, and  $L_{DiceCE}$  supplies dense pixel-level gradients to refine segmentation boundaries and stabilize training.

### 5.3.3 Effect of Semantic Probe Selection

We investigate the choice of semantic probes for the segmentation head: using a dedicated `<seg>` token versus the hidden states of the entire answer. As shown in Table 4, in Stage 1, employing the whole answer as the semantic probe yields better initial performance (32.25% vs. 30.37% mDice), likely due to its access to richer contextual semantics.

However, during RL-stage, the `<seg>` token exhibits clear advantages, achieving a final mDice of 37.06%, significantly outperforming the whole answer variant (33.01%). We attribute this improvement to two main factors. This benefit arises from two factors: (1) the token appears at the end of the sequence, enabling its hidden state to aggregate global reasoning context; and (2) being generated right after localization outputs, it naturally captures localization-aware information that aligns detection and segmentation. Furthermore, under GRPO training, using the `<seg>` tends to yield higher reward variance, providing stronger discriminative guidance for policy updates. This leads to more stable learning and ultimately better segmentation performance with fewer failures.

### 5.3.4 Backbone Scalability

We compare different SAM backbones at Stage 1 to isolate the impact of the segmentation module. Table 5 shows that MedSAM 2 [42] outperforms SAMed2D[23] and SAM 2[43], exhibiting superior robustness on our medical dataset. Thus, we adopt MedSAM 2 as the default segmentation model to

achieve optimal semantic prompting compatibility and the lowest failure rate.

## 5.4 Qualitative Analysis and Clinical Value

We present qualitative results in Fig. 5 to illustrate the benefits of our two-stage reasoning paradigm and to compare our method with representative baselines.

### 5.4.1 Progressive Improvements in Reasoning and Masks

We observe a transition from template-like reasoning in Stage 1 to more deliberate and verifiable reasoning in Stage 2, leading to more accurate masks. Stage 1 responses often mimic a CoT style but include *hallucinated* or overly confident claims, asserting visual cues without sufficient evidence, aligned with coarse or misplaced masks. In contrast, Stage 2 enables autonomous verification, the model adopts cautious language (e.g., “possible”, “could suggest”, “may indicate”) and produces grounded, correct descriptions. Consequently, the predicted masks are refined in both boundary delineation and lesion extent, with fewer false positives and improved spatial consistency. We randomly picked 200 samples for **expert review**, with senior clinicians evaluating both segmentation and reasoning results. Their assessment confirmed that Stage 2 produces clinically realistic boundaries and clear, interpretable reasoning consistent with expert judgment, demonstrating its practical applicability.

### 5.4.2 Comparison with Baselines

Compared to recent strong baselines, our method shows more robust behavior across challenging cases. MedPLIB misses small lesions and often degenerates to organ-level segmentation, while SegZero(Trained) relies heavily on bounding-box localization with error accumulation from inaccurate boxes. In contrast, our approach effectively decouples localization and segmentation. Even with imprecise boxes, it recovers correct regions via reasoning-guided refinement, delivering superior masks and higher Dice scores across modalities and targets.

## 6 Conclusion

In this paper, we explore the transition from perceptual segmentation to reasoning-driven analysis for complex medical lesions. To this end, we construct ComLesion-14K, the first large-scale benchmark specifically designed to capture challenging clinical scenarios that require explicit medical reasoning, filling a critical gap in existing datasets. To address the associated challenge, we developed CORE-Seg, an end-to-end framework with a Semantic-Guided Prompt Adapter that links medical logic to segmentation via latent

interaction. This method adopts a progressive SFT-to-GRPO training strategy equipped with an adaptive dual-granularity reward, which alleviates reward sparsity while enhancing reasoning interpretability and segmentation accuracy. Experiments show that it achieves SOTA performance and reduces the failure rate, suggesting its potential for clinical use.

Despite the encouraging results, several limitations remain. The current framework mainly targets 2D images and does not support 3D volumetric medical data, limiting its ability to exploit inter-slice context. In addition, inference can be slow due to explicit reasoning, which increases computational cost. Future work will extend the framework to volumetric segmentation and improve efficiency while maintaining accuracy and clinical reliability.

## Availability of Data and Materials

The data that support the findings of this study can be downloaded from <https://xyx1024.github.io/CORE-Seg.github.io>.

## Acknowledgements

This work was supported by the National Natural Science Foundation of China under Grant 62476054 and Grant 62576153.

## Declaration of Competing Interest

The authors have no competing interests to declare that are relevant to the content of this article.

## References

- [1] Ronneberger O, Fischer P, Brox T. U-net: Convolutional networks for biomedical image segmentation. In *International Conference on Medical image computing and computer-assisted intervention*, Springer, 2015, 234–241.
- [2] Xie Y, Zhou T, Zhou Y, Chen G. Simtxtseg: Weakly-supervised medical image segmentation with simple text cues. In *International Conference on Medical Image Computing and Computer-Assisted Intervention*, Springer, 2024, 634–644.
- [3] Isensee F, Jaeger PF, Kohl SA, Petersen J, Maier-Hein KH. nnU-Net: a self-configuring method for deep learning-based biomedical image segmentation. *Nature methods*, 2021, 18(2): 203–211.
- [4] Rahman MM, Marculescu R. Multi-scale hierarchical vision transformer with cascaded attention decoding for medical image segmentation. In *Medical Imaging with Deep Learning*, PMLR, 2024, 1526–1544.
- [5] Li C, Wong C, Zhang S, Usuyama N, Liu H, Yang J, Naumann T, Poon H, Gao J. Llava-med: Training a large language-and-vision assistant for biomedicine in one day. *Advances in Neural Information Processing Systems*, 2023, 36: 28541–28564.

- [6] Chen J, Gui C, Ouyang R, Gao A, Chen S, Chen GH, Wang X, Cai Z, Ji K, Wan X, et al.. Towards injecting medical visual knowledge into multimodal llms at scale. In *Proceedings of the 2024 conference on empirical methods in natural language processing*, 2024, 7346–7370.
- [7] Jiang S, Wang Y, Song S, Hu T, Zhou C, Pu B, Zhang Y, Yang Z, Feng Y, Zhou JT, et al.. Hulu-med: A transparent generalist model towards holistic medical vision-language understanding. *arXiv preprint arXiv:2510.08668*, 2025.
- [8] Bai S, Chen K, Liu X, Wang J, Ge W, Song S, Dang K, Wang P, Wang S, Tang J, Zhong H, Zhu Y, Yang M, Li Z, Wan J, Wang P, Ding W, Fu Z, Xu Y, Ye J, Zhang X, Xie T, Cheng Z, Zhang H, Yang Z, Xu H, Lin J. Qwen2.5-VL Technical Report. *arXiv preprint arXiv:2502.13923*, 2025.
- [9] Hurst A, Lerer A, Goucher AP, Perelman A, Ramesh A, Clark A, Ostrow A, Welihinda A, Hayes A, Radford A, et al.. Gpt-4o system card. *arXiv preprint arXiv:2410.21276*, 2024.
- [10] Tong Q, Lu Z, Liu J, Zheng Y, Lu ZM. Medisee: Reasoning-based pixel-level perception in medical images. In *Proceedings of the 33rd ACM International Conference on Multimedia*, 2025, 2742–2751.
- [11] Huang X, Shen L, Liu J, Shang F, Li H, Huang H, Yang Y. Towards a multimodal large language model with pixel-level insight for biomedicine. In *Proceedings of the AAAI Conference on Artificial Intelligence*, volume 39, 2025, 3779–3787.
- [12] Yan Z, Diao M, Yang Y, Jing R, Xu J, Zhang K, Yang L, Liu Y, Liang K, Ma Z. Medreasoner: Reinforcement learning drives reasoning grounding from clinical thought to pixel-level precision. *arXiv preprint arXiv:2508.08177*, 2025.
- [13] Huang Y, Peng Z, Zhao Y, Yang P, Yang X, Shen W. MedSeg-R: Reasoning Segmentation in Medical Images with Multimodal Large Language Models. *arXiv preprint arXiv:2506.10465*, 2025.
- [14] Zou K, Bai Y, Liu B, Chen Y, Chen Z, Zhou Y, Yuan X, Wang M, Shen X, Cao X, et al.. Uncertainty-aware medical diagnostic phrase identification and grounding. *IEEE Transactions on Pattern Analysis and Machine Intelligence*, 2025.
- [15] Lai X, Tian Z, Chen Y, Li Y, Yuan Y, Liu S, Jia J. Lisa: Reasoning segmentation via large language model. In *Proceedings of the IEEE/CVF conference on computer vision and pattern recognition*, 2024, 9579–9589.
- [16] Liu Y, Peng B, Zhong Z, Yue Z, Lu F, Yu B, Jia J. Seg-zero: Reasoning-chain guided segmentation via cognitive reinforcement. *arXiv preprint arXiv:2503.06520*, 2025.
- [17] Shao Z, Wang P, Zhu Q, Xu R, Song J, Bi X, Zhang H, Zhang M, Li Y, Wu Y, et al.. Deepseekmath: Pushing the limits of mathematical reasoning in open language models. *arXiv preprint arXiv:2402.03300*, 2024.
- [18] Kirillov A, Mintun E, Ravi N, Mao H, Rolland C, Gustafson L, Xiao T, Whitehead S, Berg AC, Lo WY, et al.. Segment anything. In *Proceedings of the IEEE/CVF international conference on computer vision*, 2023, 4015–4026.
- [19] Hu R, Zhu L, Zhang Y, Cheng T, Liu L, Liu H, Ran L, Chen X, Liu W, Wang X. GroundingSuite: Measuring Complex Multi-Granular Pixel Grounding. In *Proceedings of the IEEE/CVF International Conference on Computer Vision*, 2025, 23105–23114.
- [20] Zhang X, Wu C, Zhao Z, Lin W, Zhang Y, Wang Y, Xie W. Pmc-vqa: Visual instruction tuning for medical visual question answering. *arXiv preprint arXiv:2305.10415*, 2023.
- [21] Hu Y, Li T, Lu Q, Shao W, He J, Qiao Y, Luo P. Omnimedvqa: A new large-scale comprehensive evaluation benchmark for medical lvlm. In *Proceedings of the IEEE/CVF Conference on Computer Vision and Pattern Recognition*, 2024, 22170–22183.
- [22] Wu R, Yao Y, Ma T, Zhang C, Su N, Zhou T, Chen G, Fan W, Zhou Y. Bridging the Gap in Ophthalmic AI: MM-Retinal-Reason Dataset and OphthaReason Model toward Dynamic Multimodal Reasoning. *arXiv preprint arXiv:2508.16129*, 2025.
- [23] Ye J, Cheng J, Chen J, Deng Z, Li T, Wang H, Su Y, Huang Z, Chen J, Jiang L, et al.. Sa-med2d-20m dataset: Segment anything in 2d medical imaging with 20 million masks. *arXiv preprint arXiv:2311.11969*, 2023.
- [24] Cheng J, Fu B, Ye J, Wang G, Li T, Wang H, Li R, Yao H, Cheng J, Li J, et al.. Interactive medical image segmentation: A benchmark dataset and baseline. In *Proceedings of the Computer Vision and Pattern Recognition Conference*, 2025, 20841–20851.
- [25] Zhao T, Gu Y, Yang J, Usuyama N, Lee HH, Kiblawi S, Naumann T, Gao J, Crabtree A, Abel J, et al.. A foundation model for joint segmentation, detection and recognition of biomedical objects across nine modalities. *Nature methods*, 2025, 22(1): 166–176.
- [26] Radford A, Kim JW, Hallacy C, Ramesh A, Goh G, Agarwal S, Sastry G, Askell A, Mishkin P, Clark J, et al.. Learning transferable visual models from natural language supervision. In *International conference on machine learning*, PmlR, 2021, 8748–8763.
- [27] Liu J, Zhang Y, Chen JN, Xiao J, Lu Y, A Landman B, Yuan Y, Yuille A, Tang Y, Zhou Z. Clip-driven universal model for organ segmentation and tumor detection. In *Proceedings of the IEEE/CVF international conference on computer vision*, 2023, 21152–21164.
- [28] Gu Y, Cheng Y, Chen CLP, Wang X. Proximal Policy Optimization With Policy Feedback. *IEEE Transactions on Systems, Man, and Cybernetics: Systems*, 2022, 52(7): 4600–4610, doi:10.1109/TSMC.2021.3098451.
- [29] Rafailov R, Sharma A, Mitchell E, Manning CD, Ermon S, Finn C. Direct preference optimization: Your language model is secretly a reward model. *Advances in neural information processing systems*, 2023, 36: 53728–53741.
- [30] Huang J, et al.. SAM-R1: Leveraging SAM for Reward Feedback in Multimodal Segmentation via Reinforcement Learning. *arXiv preprint arXiv:2505.22596*, 2025.
- [31] Zhu L, Ouyang B, Zhang Y, Cheng T, Hu R, Shen H, Ran



- L, Chen X, Yu L, Liu W, et al.. Lens: Learning to segment anything with unified reinforced reasoning. *arXiv preprint arXiv:2508.14153*, 2025.
- [32] Clauset A, Shalizi CR, Newman ME. Power-law distributions in empirical data. *SIAM review*, 2009, 51(4): 661–703.
- [33] Satopaa V, Albrecht J, Irwin D, Raghavan B. Finding a” knee” in a haystack: Detecting knee points in system behavior. In *2011 31st international conference on distributed computing systems workshops*, IEEE, 2011, 166–171.
- [34] Zhou J, Jia X, Ni D, Noble A, Huang R, Tan T, Van MT. Thyroid Nodule Segmentation and Classification in Ultrasound Images, 2020, doi:10.5281/zenodo.3715942.
- [35] Chitalia R, Pati S, Bhalerao M, Thakur S, Jahani N, Belenky J, McDonald E, Gibbs J, Newitt D, Hylton N, et al.. Expert tumor annotations and radiomic features for the ispy1/acrin 6657 trial data collection. *The Cancer Imaging Archive*, 2022.
- [36] Bernal J, Sánchez FJ, Fernández-Esparrach G, Gil D, Rodríguez C, Vilarinho F. WM-DOVA maps for accurate polyp highlighting in colonoscopy: Validation vs. saliency maps from physicians. *Computerized medical imaging and graphics*, 2015, 43: 99–111.
- [37] Zhu J, Wang W, Chen Z, Liu Z, Ye S, Gu L, Tian H, Duan Y, Su W, Shao J, et al.. Internvl3: Exploring advanced training and test-time recipes for open-source multimodal models. *arXiv preprint arXiv:2504.10479*, 2025.
- [38] Sun H, Jiang Y, Lou W, Zhang Y, Li W, Wang L, Liu M, Liu L, Wang X. Chiron-o1: Igniting Multimodal Large Language Models towards Generalizable Medical Reasoning via Mentor-Intern Collaborative Search. In *The Thirty-ninth Annual Conference on Neural Information Processing Systems*, 2025.
- [39] Xu W, Chan HP, Li L, Aljunied M, Yuan R, Wang J, Xiao C, Chen G, Liu C, Li Z, et al.. Lingshu: A Generalist Foundation Model for Unified Multimodal Medical Understanding and Reasoning. *arXiv preprint arXiv:2506.07044*, 2025.
- [40] Sellergren A, Kazemzadeh S, Jaroensri T, Kiraly A, Traverse M, Kohlberger T, Xu S, Jamil F, Hughes C, Lau C, et al.. Medgemma technical report. *arXiv preprint arXiv:2507.05201*, 2025.
- [41] Shen H, Liu P, Li J, Fang C, Ma Y, Liao J, Shen Q, Zhang Z, Zhao K, Zhang Q, et al.. Vlm-r1: A stable and generalizable r1-style large vision-language model. *arXiv preprint arXiv:2504.07615*, 2025.
- [42] Ma J, Yang Z, Kim S, Chen B, Baharoon M, Fallahpour A, Asakereh R, Lyu H, Wang B. Medsam2: Segment anything in 3d medical images and videos. *arXiv preprint arXiv:2504.03600*, 2025.
- [43] Ravi N, Gabeur V, Hu YT, Hu R, Ryali C, Ma T, Khedr H, Rädle R, Rolland C, Gustafson L, et al.. SAM 2: Segment Anything in Images and Videos. In *International Conference on Learning Representations*, volume 2025, 2025, 28085–28128.